Closed-loop 3D path following of scaled-up helical microswimmers

Ali Oulmas[1,2], Nicolas Andreff[2] and Stéphane Régnier[1]

Abstract— This paper addresses the problem of 3D path following of magnetic helical microswimmers in closed-loop. An error kinematic model in a local frame with sideslip and attack angles is used to express the motion of the helical microswimmer. A new derivation of the chained form with three inputs and five states is used to linearize the kinematic model in order to design a decoupled stable control. In experimentation, the 3D path following is validated using a scaled-up magnetic helical microswimmer with visual servo control by following first a spatial straight line, then a helix trajectory and finally an inclined sinusoidal trajectory. The closed-loop control is also compared with the open-loop control to illustrate the robustness and the accuracy of both controllers to the disturbances.

I. INTRODUCTION

Magnetic helical microswimmers present solutions to several applications thanks to their microsize which gives them the possibility of accessing complex environments. Since the human body is transparent to magnetic fields, they can give rise to minimally invasive medicine [1] such as targeted drug delivery [2]. In the industrial area, microswimmers can be used to sort, assemble and transport microobjects [3].

At low scale, swimming is characterized by low Reynolds numbers ($Re << 1$) because viscosity forces dominate over inertia forces. Consequently, reciprocal movement is not suitable [4]. Helical microswimmers use a nonreciprocal motion that consists of combining a corkscrew tail and a rotating magnetic field in order to transform the rotary motion into linear motion, like E. coli bacteria.

Most often, the task to be performed by a microswimmer will be defined as a geometric path to follow, without any specification of the velocity profile along that task, e.g. through the drawing by a non-roboticist of a curve in the workspace. In the mobile robotics community, this is referred to as *path following* in opposition to *trajectory tracking*.
In this work, we focus on path following because it has better performance with smoother convergence to the path [5].

In the literature, many researchers demonstrated a motion control of microswimmers in plane and space using open-loop control. For instance, [6] presented a curved U-turn trajectory following with gravity compensation in the vertical plane using a helical swimmer. Navigation in space using a helical microswimmer was shown in [3] for pick-and-place tasking. However during disturbances such as boundary effects [7] or strong flow in blood vessel, the microswimmer

drifts from the desired path and this results in a non-accurate motion. To overcome the problem, Xu *et al.* proposed a closed-loop control in [9] by following a straight line in the horizontal plane with an altitude controlled in open-loop using a scaled-up helical microswimmer. However, the kinematic model developed in [9] is for planar path following and is not adapted to following a path in 3D space.

This paper is motivated particularly by the applications in 3D space for 5-DOF manipulation of biological cells, for example inside human body where the 3D control in closed-loop is necessary to bring the swimmer with high precision to specific locations. Therefore, the contribution of this paper is to extend the kinematic model in [9] to a general path following algorithm taking into account the gravity compensation and lateral disturbances. We model the microswimmer in a local frame using the Serret-Frenet frame with sideslip and attack angles. The desired motion will be expressed in terms of path parameters (curvilinear abscissa, curvature, torsion ...). A new derivation of the chained form with five states and three inputs will be used to linearize the model in order to design a decoupled stable controller. Thus, the kinematic model in [9] will become a subset of our general form model.

This approach is validated in experiments using a scaled-up helical microswimmer (SHM) by following curves with different curvatures and inclinations. The lateral displacements caused mainly by boundary effects [7] and thermal noises [10] are considered as disturbances. Moreover, the apparent weight which is defined as the resultant of the gravity and buoyancy forces is nonzero, thus creates a downward drift [6]. The closed-loop control aims to correct the drifting errors. In order to illustrate its accuracy and robustness to these disturbances, the closed-loop control is compared with the open-loop control.

This paper is organized as follows: section II describes the 3D error kinematic model of the helical swimmer using the Serret-Frenet frame with sideslip and attack angles. Then, section III shows the conversion of the kinematic model into the chained form and the control law that allows the 3D path following. Section IV presents the magnetic manipulation system used to steer the helical swimmer wirelessly. Section V shows the results obtained by applying the 3D visual servo control on the prototype.

II. 3D KINEMATIC MODEL OF THE HELICAL SWIMMER

To control the helical swimmer, an error kinematic model with the Serret-Frenet frame associated to the reference path is used to express the desired motion in terms of the path parameters. Besides, helical swimmers can be considered as

[1]A. Oulmas and S. Régnier are with Institut des Systémes Intelligents et Robotique, University of Pierre & Marie Curie, 75005 Paris, France `ali.oulmas@isir.upmc.fr`, `stephane.regnier@upmc.fr`
[2]A. Oulmas and N. Andreff are with FEMTO-ST Institute, CNRS/University of Franche-Comté/ENSMM/UTBM, 25000 Besançon, France `nicolas.andreff@femto-st.fr`

autonomous vehicles with nonholonomic constraints, since they advance in the direction of their axis by converting the rotary motion into linear motion.

The kinematics of the helical swimmer with nonholonomic constraints are developed using an absolute global frame $\mathbf{U} = \{\ \mathbf{x}\ \ \mathbf{y}\ \ \mathbf{z}\ \}$ with origin $\mathbf{O}$ and a moving body frame $\mathbf{B_h} = \{\ \mathbf{x_B}\ \ \mathbf{y_B}\ \ \mathbf{z_B}\}$ attached to the body of the swimmer located at $\mathbf{G}$ the center of mass of the swimmer. The movement of the swimmer is characterized by the inclination angle θ_i and the direction angle θ_d. The first angle is formed between the horizontal plane $\mathbf{x}\mathbf{O}\mathbf{y}$ and the axis of the swimmer and the second angle is built between the $\mathbf{x}$ axis and the axis of the swimmer projected in the horizontal plane $\mathbf{x}\mathbf{O}\mathbf{y}$.

In order to compensate the weight of the swimmer and lateral deviations mentioned above, the so-called wind frame $\mathbf{W} = \{\ \mathbf{x_w}\ \ \mathbf{y_w}\ \ \mathbf{z_w}\ \}$ is introduced [11]. The $\mathbf{x_w}$ axis is aligned with the total linear velocity v of the helical swimmer as shown in Fig. 1. The frame $\mathbf{W}$ is obtained by rotating the $\mathbf{B_h}$ frame around $\mathbf{y_B}$ through the attack angle α, then around $\mathbf{z_B}$ through the sideslip angle β.

The path to be followed is denoted by $\mathscr{C}(s)$ which is described with the curvilinear coordinate s, the curvature and torsion of the path respectively c and τ.

$\mathbf{F} = \{\ \mathbf{x_F}\ \ \mathbf{y_F}\ \ \mathbf{z_F}\ \}$ is the Serret-Frenet frame that moves along the path $\mathscr{C}(s)$. $\mathbf{x_F}$ and $\mathbf{y_F}$ are respectively the tangent and the normal to the path while $\mathbf{z_F}$ represents the binormal to the path and is given by the cross product of $\mathbf{x_F}$ and $\mathbf{y_F}$. $\mathbf{F}$ is characterized by the reference direction angle θ_{dc} and the reference inclination angle θ_{ic}

The goal of path following is to drive the linear distance and orientation errors to zero. For that purpose, the following state vector is defined:

$$\mathbf{q} = \begin{bmatrix} s \\ d_y \\ \theta_{de} \\ d_z \\ \theta_{ie} \end{bmatrix} = \begin{bmatrix} s \\ d_y \\ \theta_d - \beta - \theta_{dc} \\ d_z \\ \theta_i - \alpha - \theta_{ic} \end{bmatrix} \qquad (1)$$

where d_y and d_z represent respectively the vertical and horizontal distances between the swimmer center of mass $\mathbf{G}$ and the point $\mathbf{S}$ closest to the path while θ_{de} and θ_{ie} represent respectively the direction and inclination angles errors.

The control inputs are the total linear velocity v for driving and the angular velocities Ω_y and Ω_z for steering:

$$\mathbf{m} = \begin{bmatrix} v \\ \Omega_y \\ \Omega_z \end{bmatrix} \qquad (2)$$

As the propulsion of the helical swimmer is external, the angular velocity Ω_x along the swimmer axis is not considered. In addition, the error in roll does not perturb the path following [12]. The number of inputs is less than the number of degrees of freedom, which is a characteristic of a nonholonomic system.

The position $^{\mathbf{U}}\mathbf{G_W}$ of the helical swimmer in the global frame $\mathbf{U}$ can be expressed as shown in Fig. 1 by:

$$^{\mathbf{U}}\mathbf{G_W} = {}^{\mathbf{U}}\mathbf{S_F} + {}^{\mathbf{U}}\mathbf{R_F}\,{}^{\mathbf{F}}\mathbf{G_W} \qquad (3)$$
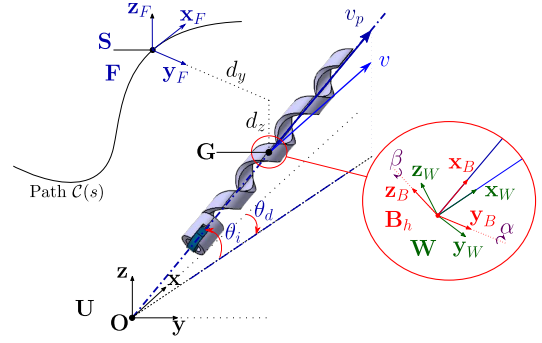

Fig. 1: 3D Path following of the helical swimmer.

where $^{\mathbf{U}}\mathbf{R_F}$ is the rotation matrix from $\mathbf{F}$ to $\mathbf{U}$ and $^{\mathbf{U}}\mathbf{S_F}$ is the closest point on the path expressed in the global frame $\mathbf{U}$. Differentiating (3) with respect to the time and expressing it in the Serret-Frenet frame gives:

$$^{\mathbf{F}}\mathbf{R_W}\,{}^{\mathbf{W}}\mathbf{v_W} = {}^{\mathbf{F}}\mathbf{v_F} + {}^{\mathbf{F}}\dot{\mathbf{G}}_{\mathbf{W}} + {}^{\mathbf{F}}\boldsymbol{\omega}_{\mathbf{F}} \times {}^{\mathbf{F}}\mathbf{G_W} \qquad (4)$$

where $^{\mathbf{F}}\mathbf{R_W}$ is the rotation matrix from $\mathbf{W}$ to $\mathbf{B}$ using Euler angles characterized by θ_{de} and θ_{ie} while $^{\mathbf{F}}\mathbf{v_F}$ and $^{\mathbf{F}}\boldsymbol{\omega}_{\mathbf{F}}$ are the linear and angular velocities of frame $\mathbf{F}$ expressed in itself.

The relative angular velocity between the Serret-Frenet frame $\mathbf{F}$ and $\mathbf{W}$, expressed in frame $\mathbf{W}$ is given by:

$$^{\mathbf{W}}\boldsymbol{\omega}^{\mathbf{r}}_{\mathbf{W,F}} = {}^{\mathbf{W}}\boldsymbol{\omega}_{\mathbf{W}} - {}^{\mathbf{W}}\boldsymbol{\omega}_{\mathbf{F}} \qquad (5)$$

Following [12] and using (4) and (5), the 3D error kinematic model of the helical swimmer can be expressed as:

$$\begin{cases} \dot{s} &= \dfrac{v\,C\theta_{de}\,C\theta_{ie}}{1 - c\,d_y} \\[2mm] \dot{d}_y &= v\,S\theta_{de}\,C\theta_{ie} + \tau\,d_z\,\dot{s} \\[2mm] \dot{d}_z &= -v\,S\theta_{ie} - \tau\,d_y\,\dot{s} \\[2mm] \dot{\theta}_{ie} &= \Omega_y\,C\beta - \Omega_z\,S\beta\,S\alpha - \dot{\alpha}\,C\beta + \tau\,\dot{s}\,S\theta_{de} \\[2mm] \dot{\theta}_{de} &= \Omega_z\,\dfrac{C\alpha}{C\theta_{ie}} + \dfrac{\dot{\beta}}{C\theta_{ie}} - \tau\,\dot{s}\,T\theta_{ie}\,C\theta_{de} - c\,\dot{s} \end{cases} \qquad (6)$$

For ease of notation, we defined $C\cdot = \cos(\cdot)$, $S\cdot = \sin(\cdot)$ and $T\cdot = \tan(\cdot)$. To check the validity of this model, we calculated the projection of these equations in the horizontal plane setting the variables d_z, τ, α, θ_{ie} and Ω_y to zero, which gave us the kinematic model used by Xu in [9] and Samson in [13] for the planar path following of mobile robots.

III. CHAINED FORM AND CONTROL LAW

A. Chained form

The total linear velocity v of the helical swimmer is not aligned with the propulsion velocity v_p because of the weight and lateral disturbances [6]. Therefore, to drive the microswimmer to the path, the total linear velocity v should be aligned with the tangent of the reference path. In other words, the distances d_y and d_z and the orientations θ_{de} and θ_{ie} must be servoed to zero. For that purpose, a stable control law is necessary:

$$(v,\ \Omega_y,\ \Omega_z) = f(d_y,\ d_z,\ \theta_{ie},\ \theta_{de}) \qquad (7)$$

The kinematic model of the helical swimmer formed by (6) is nonlinear. In order to control this kind of system, a solution consists in linearizing it around the equilibrium $d_y = d_z = \theta_{de} = \theta_{ie} = 0$. Samson has established an approach to convert the models of planar mobile robots (unicycle, car-like, with trailers) into linear models using a chained form with two inputs and three states [13]. The conversion of multi-inputs nonholonomic systems into the chained form is presented in [14] for the fire truck example. Inspired by [13], [14] and [15], we propose converting the kinematic model of the helical swimmer into the following chained form with three inputs and five states:

$$\dot{x}_1 = u_1, \quad \dot{x}_2 = x_3\, u_1, \quad \dot{x}_3 = u_2,$$
$$\dot{x}_4 = x_5\, u_1, \quad \dot{x}_5 = u_3 \tag{8}$$

where $\mathbf{x} = (x_1, x_2, x_3, x_4, x_5)^T$ is the state vector and $\mathbf{u} = (u_1, u_2, u_3)^T$ is the input vector. The transformations of (6) into the chained form are defined as:

$$\begin{aligned}
x_1 &= s \\
x_2 &= d_y \\
x_3 &= (1 - c\, d_y)\, T\theta_{de} + \tau\, d_z \\
x_4 &= d_z \\
x_5 &= (c\, d_y - 1)\, T\theta_{ie}\, C(\theta_{de})^{-1} - \tau\, d_y
\end{aligned} \tag{9}$$

and,

$$\begin{aligned}
u_1 &= \dot{s} \\
u_2 &= \gamma_{21}\, \Omega_z + \gamma_{22} \\
u_3 &= \gamma_{31}\, \Omega_y + \gamma_{32}\, \Omega_z + \gamma_{33}
\end{aligned} \tag{10}$$

where γ_{21}, γ_{22}, γ_{31}, γ_{32} and γ_{33} are scalars and are given in the Appendix.

Therefore, the derivative of $x_{i=1,..5}$ with respect to the curvilinear abscissa s defines a system independent of the total linear velocity v of the helical swimmer as follows:

$$x_1' = 1, \quad x_2' = x_3, \quad x_3' = u_{12}$$
$$x_4' = x_5, \quad x_5' = u_{13} \tag{11}$$

with: $x_3' = \frac{\dot{x}_3}{\dot{s}} = \frac{u_2}{u_1} \overset{def}{=} u_{12}$ and $x_5' = \frac{\dot{x}_5}{\dot{s}} = \frac{u_3}{u_1} \overset{def}{=} u_{13}$.
The model (11) is clearly linear and time invariant (LTI) and depends on the auxiliary control inputs u_{12} and u_{13}.

B. Control

To reach and pursue the path, a simple state feedback control law is used as follows:

$$\begin{cases} u_{12} = -k_{d1}\, x_2 - k_{t1}\, x_3 \\ u_{13} = -k_{d2}\, x_4 - k_{t2}\, x_5 \end{cases} \tag{12}$$

where k_{t1}, k_{d1}, k_{t2} and k_{d2} are the control gains and are strictly positive. The closed-loop performance can be adjusted using these parameters.

Replacing (8) in (12) gives two decoupled 1-dimensional 2nd order systems:

$$\begin{cases} x_2'' + k_{t1}\, x_2' + k_{d1}\, x_2 &= 0 \\ x_4'' + k_{t2}\, x_4' + k_{d2}\, x_4 &= 0 \end{cases} \tag{13}$$

that independently converge to zero under appropriate gain tuning.

Finally, using (9) leads to the convergence of the distances d_y and d_z and the orientations θ_{ie} and θ_{de} to zero. Thus, a spatial path following is achieved.

C. Actuation

By knowing the position of the helical swimmer $\mathbf{G}$ and the path parameters (curvilinear abscissa, curvature and torsion), the control law on the steering angular velocities Ω_y and Ω_z is computed using (10) and the new control (12) as follows:

$$\begin{cases} \Omega_z = (u_2 - \gamma_{22})\, \gamma_{21}^{-1} \\ \Omega_y = \left(u_3 - \gamma_{33} - \gamma_{32}\, \gamma_{21}^{-1}\, (u_2 - \gamma_{22}) \right)\, \gamma_{31}^{-1} \end{cases} \tag{14}$$

with

$$\begin{aligned}
u_2 &= u_1\, u_{12} \\
&= \dot{s} \left(-k_{d1}\, d_y - k_{t1}\, (\tau\, d_z + (1 - c\, d_y)\, T\theta_{de}) \right)
\end{aligned}$$

and

$$\begin{aligned}
u_3 &= u_1\, u_{13} \\
&= \dot{s} \left(-k_{d2}\, d_z + k_{t1}\, (\tau\, d_y - (c\, d_y - 1)\, C(\theta_{de})^{-1}\, T\theta_{ie}) \right)
\end{aligned}$$

where $\dot{s}$ is given in (6). The controller is asymptotically stable when $u_1 = \dot{s}$, the velocity along the path, is constant. In addition, the path following and the total linear velocity are decoupled, which is suitable for low Reynolds number environments in order to overcome obstacles and disturbances with more accuracy [9].
As far as we know, the control law for 3D path following of a helical swimmer in closed-loop is proposed for the first time.

IV. MAGNETIC MANIPULATION SYSTEM

The proposed control law for 3D path following was experimentally tested using a scaled-up helical microswimmer (SHM) with 14 mm length and 1 mm in diameter. The use of the SHM facilitates the observation using regular optical devices. In addition, the fabrication in large scale is easier using a 3D printer. It also highlights the ability of compensating drift (the weight, microfluidic flow at lower scale).

In order to actuate the SHM wirelessly in space, a non contact magnetic system composed of three pairs of coils in Helmholtz configuration is used to generate a uniform rotating magnetic field in the center of the workspace (Fig. 2). The magnetic torque $\mathbf{T}$ applied on the helical swimmer is given by:

$$\mathbf{T} = \mathbf{M} \times \mathbf{B} \tag{15}$$

where $\mathbf{M}$ is the magnetic moment of the SHM and $\mathbf{B}$ the magnetic field. The magnetic torque tends to align the magnetic moment with the applied magnetic field. Therefore, with a rotating magnetic field and a helical tail, the SHM can advance by converting its self-rotation into linear motion.

The magnetic field can be decomposed into a magnetic field $\mathbf{B}_\perp$ perpendicular to the SHM axis and a magnetic field $\mathbf{B}_\parallel$ parallel to the SHM axis [8]. The first vector yields the open-loop self-rotation of the SHM and is given by:

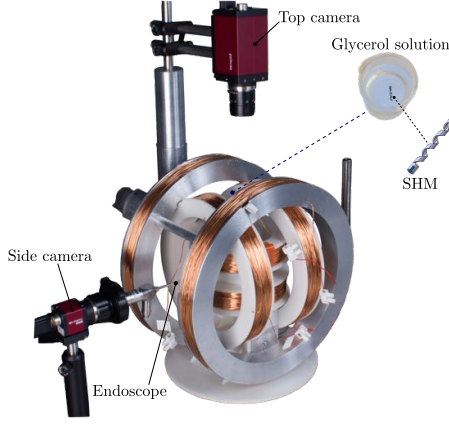$$\mathbf{B}_\perp = B_0\, \cos(2\pi f t)\, \tilde{\mathbf{u}} + B_0\, \sin(2\pi f t)\, \tilde{\mathbf{v}} \tag{16}$$

Fig. 2: Magnetic manipulation system.

Fig. 3: The 3D straight line following with the control gains of $k_{t1} = 0.01$, $k_{d1} = 0.2$, $k_{t2} = 0.2$ and $k_{d2} = 0.3$.

where B_0 is the magnetic flux density in the center of the workspace and $\tilde{\mathbf{u}}$ and $\tilde{\mathbf{v}}$ are the basis vectors of the plane perpendicular to the axis of the SHM.

The second vector yields the steering of the SHM in order to reach the target orientation and can be expressed as [8]:

$$\mathbf{B}_\parallel = -sign(\mathbf{B}_\perp \; \mathbf{n}^*) \; \lambda \; \parallel \mathbf{n} \times \mathbf{n}^* \parallel \mathbf{n} \qquad (17)$$

where $\mathbf{n}$ and $\mathbf{n}^*$ are respectively the real-time and desired orientations of the SHM and λ is the control gain. The tuning of this gain is empirical.

The position $\mathbf{G}$ and orientations of the swimmer are reconstructed by stereovision. The SHM axis $\mathbf{n}$ is related to the direction and inclination angles as follows:

$$\mathbf{n} = \begin{bmatrix} S\theta_i & C\theta_i S\theta_d & C\theta_i C\theta_d \end{bmatrix}^T \qquad (18)$$

$\mathbf{B}_\parallel$ is thus the "actuator" associated to the steering angular velocities Ω_z and Ω_y in (14), which are related to the desired inclination and direction angles as follows:

$$\begin{cases} \theta_d^*(t) = \theta_d(t) + \Omega_z \, dt \\ \theta_i^*(t) = \theta_i(t) + \Omega_y \, dt \end{cases} \qquad (19)$$

which is transformed into $\mathbf{n}^*$ and fed into (18).

The total linear velocity of the helical swimmer is defined as the linear velocity along the $\mathbf{x_w}$ axis of the wind frame $\mathbf{W}$ which is given as:

$$v = \frac{1}{C\alpha C\beta} v_p \qquad (20)$$

where α and β are respectively the sideslip and attack angles while v_p is the propulsion velocity along the swimmer axis $\mathbf{x_B}$, defined thanks to the so-called propulsion matrix [16].

V. Experimental results

A. 3D straight line

In this section, the 3D visual servo control developed above is first tested on the prototype by following a horizontal straight line. In this case, both the torsion and curvature of the path are zero. The swimmer rotates in synchronization with the rotating magnetic field at a frequency of $f = 3.2 \; Hz$.
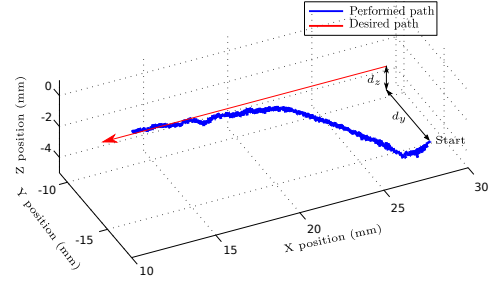
Fig. 3 depicts the 3D path followed by the SHM. The reference path is drawn by a red line and the performed path is in blue. Fig. 4 contains the horizontal and vertical projections of theses paths.

The SHM is placed at a distance $d_y = 4.4 \; mm$ and $d_z = 3 \; mm$ from the path with an initial orientation different from zero in order to see how the SHM reacts to the large distances. The multimedia attachment Video S1 shows the top and side views of the straight line following of the swimmer.

As can be seen in Fig. 3, the swimmer converges first to the reference path, then pursues the along of the path.

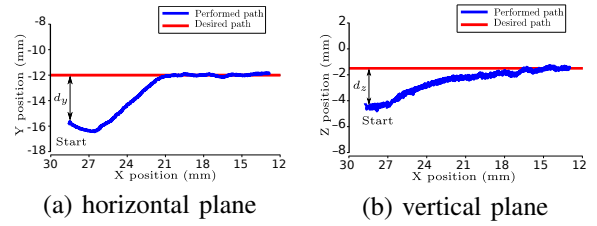

(a) horizontal plane   (b) vertical plane

Fig. 4: The 3D straight line following.

When the swimmer reaches the desired path, the distances d_z and d_y are maintained at zero. In the straight line following realized by Xu in [9], the swimmer regulates the lateral error to zero while the altitude is controlled in open-loop. However, using the 3D controller proposed here, both the altitude error and the lateral error are regulated to zero.

In the next section, a curve with constant curvature and torsion will be tested.

B. Helix trajectory

A helix trajectory is generated in order to evaluate the controller and the behavior of the swimmer on this kind of path. The swimmer was initially placed near the desired path. Fig. 5 plots the result of the 3D reconstruction by vision of the SHM position and compares it to the reference path.

It can be noted that the swimmer follows the helix trajectory despite the complexity of the path. The tracked swimmer path in the horizontal and vertical planes is presented in Fig. 6. Furthermore, the distance and orientation errors are given in Fig. 7.
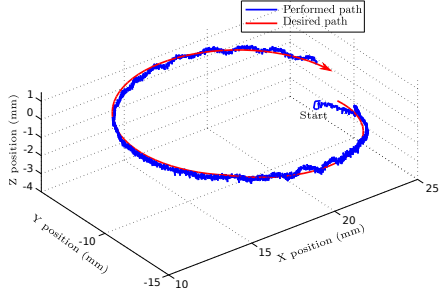
Fig. 5: The 3D reconstruction of the trajectory drawn by the SHM while following a helix trajectory with the control gains of $k_{t1} = 0.004$, $k_{d1} = 0.05$, $k_{t2} = 0.3$ and $k_{d2} = 0.09$.

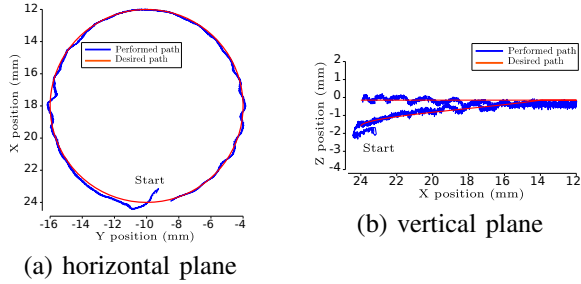(a) horizontal plane

(b) vertical plane

Fig. 6: The helix trajectory following.

The distance error d_z is maintained to zero, as well as the inclination orientation error θ_{ie} in Fig. 7.b. However, the distance error d_y is also maintained to zero but the direction orientation error θ_{de} is not zero, as shown in Fig. 7.b. This can be explained by the fact that the environment presents many lateral disturbances. The closed-loop control compensates these disturbances by increasing the direction angle. To estimate the accuracy, we compute the root-mean-
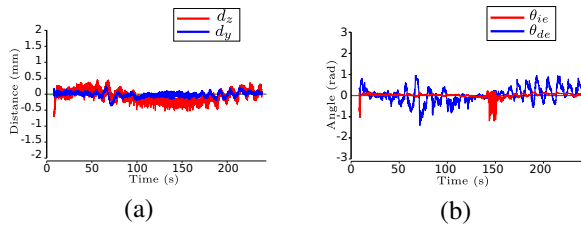

(a)

(b)

Fig. 7: Evolution of the distance errors (a) and the orientation errors (b) during the helix trajectory following.

square (RMS) and standard deviation (SD) errors (TABLE I). It can be seen that the accuracy of the path following is submillimetric (1.4 % of the body length).

TABLE I: The helix trajectory errors.

Errors	d_y (μm)	d_z (μm)	θ_{de} (rad)	θ_{ie} (rad)
RMS	83.4	199	0.349	0.151
SD	82.6	189	0.348	0.117

C. Inclined sinusoidal trajectory

Secondly, the controller was also evaluated in a more complicated curve with variable curvature and inclination by following an inclined sinusoidal trajectory. The 3D reconstruction by vision of the SHM position is given in Fig 8.
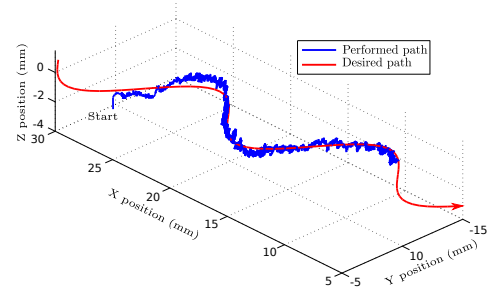

Fig. 8: The 3D reconstruction of the trajectory drawn by the SHM while following an inclined sinusoidal trajectory with the control gains of $k_{t1} = 0.04$, $k_{d1} = 0.05$, $k_{t2} = 0.05$ and $k_{d2} = 0.08$.

The tracked swimmer path in the horizontal and vertical planes is presented in Fig. 9.
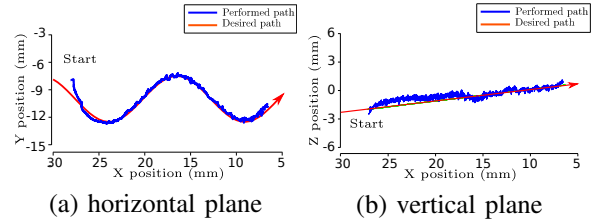

(a) horizontal plane

(b) vertical plane

Fig. 9: The tracked SHM path while following an inclined sinusoidal trajectory.

The multimedia attachment Video S2 shows the top and side views of the inclined sinusoidal trajectory following of the SHM. The swimmer follows along the path despite the succession and complexity of curvatures. The distance RMS errors during the trajectory following are 178 μm for d_y and 396 μm for d_z. The path following is still efficient.

In the next section, an experiment demonstrating the effect of the lateral disturbances and the weight of the SHM in the path following using the open-loop and closed-loop controls is presented.

D. Open-loop vs closed-loop

The performance of the 3D control of the SHM depends on the viscosity of the liquid, which in turn depends on the temperature and also on the boundary effects caused by the beaker wall. To illustrate the second effect, an open-loop control is developed and compared with the closed-loop control.

The swimmer is placed on the path without initial orientation error. The desired path is along the **x** axis with a constant altitude. In the horizontal plane (Fig. 10.a), the

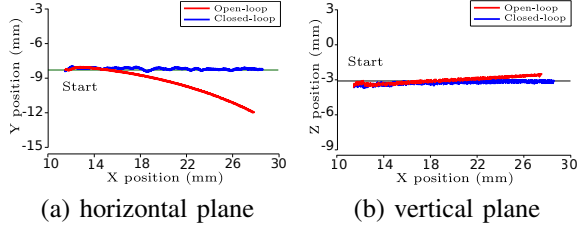(a) horizontal plane   (b) vertical plane

Fig. 10: Comparison between the open-loop control and the visual servo control.

SHM advances along the **x** axis and we observe that using the open-loop control, the SHM drifts from the reference path because of lateral disturbances caused mainly by the boundary effect, the friction between the swimmer and the substrate, and the imperfection of the system. The error is not corrected later. On the other hand, the closed loop control shows better performance despite the disturbances. The swimmer pursues the path with more precision. The errors during the closed-loop control are: $\text{RMS}(d_y) = 69.5\ \mu m$ and $\text{SD}(d_y) = 69.4\ \mu m$.

Concerning the altitude regulation in the vertical plane (Fig. 10.b), the open loop control presents some overshoot at the end of the trajectory whereas the closed loop control regulates the altitude with more precision. The errors are: $\text{RMS}(d_z) = 198.7\ \mu m$ and $\text{SD}(d_z) = 182.5\ \mu m$. As a conclusion, the closed loop control presents better performances in terms of precision in the presence of disturbances. At low scales, the proposed approach could be interesting to overcome the high flow in blood vessels or avoid obstacles and transport microobjects accurately in lab-on-chips tasks.

VI. CONCLUSIONS

We have introduced a new approach to achieve, for the first time, a 3D path following of a scaled-up helical microswimmer in closed-loop. The kinematic model of the SHM was expressed in a local frame using the Serret-Frenet frame with a new chained formulation to realize the control. The method was validated and analyzed through experimental results by following different curves (spatial straight line, helix and inclined sinusoidal trajectories). This work presents a robust solution to compensate the disturbances such as the boundary effects which are significant at low scales.

APPENDIX

Here, we define the different parameters used in section III to compute the inputs u_2 and u_3 in (10) :

$$\gamma_{21} = (1 - c\,d_y)\,C\alpha\,(C\theta_{de})^{-2}\,(C\theta_{ie})^{-1}$$

$$\gamma_{22} = \dot{\beta}\,(1 - c\,d_y)\,(C\theta_{de})^{-2}\,(C\theta_{ie})^{-1} + \frac{v}{-1 + c\,d_y}\left(C\theta_{ie}\right.$$
$$\left(\frac{c\,(c\,d_y - 1)}{C\theta_{de}}\left(C(\theta_{de})^2 - 2\right) + \left(c\,\tau\,d_z + d_y\frac{dc}{ds}\right)S\theta_{de}\right)$$
$$+ \left(\tau^2 d_y - d_z\frac{d\tau}{ds}\right)C\theta_{de}\,C\theta_{ie} + 2\,\tau(1 - c\,d_y)\,S\theta_{ie}\right)$$

$$\gamma_{31} = (-1 + c\,d_y)\,C\beta\,C(\theta_{de})^{-1}\,C(\theta_{ie})^{-2}$$

$$\gamma_{32} = (1 - c\,d_y)\,(C\theta_{de})^{-1}\,(C\theta_{ie})^{-2}\left(S\alpha\,S\beta - C\alpha\,S\theta_{ie}\,T\theta_{de}\right)$$

$$\gamma_{33} = (1 - c\,d_y)\left(\dot{\alpha}\,C\beta - \dot{\beta}\,S\theta_{ie}\,T\theta_{de}\right) - \frac{v\,C\theta_{ie}}{1 - c\,d_y}\left(d_y\,C\theta_{de}\frac{d\tau}{ds}\right.$$

$$\left. -d_y\,T\theta_{ie}\frac{dc}{ds} + \left(d_z\,\tau + 2(1 - c\,d_y)\,T\theta_{de}\right)\left(\tau\,C\theta_{de} + c\,T\theta_{ie}\right)\right)$$

γ_{22} depends on v and $\dot{\beta}$ while γ_{33} depends on v, $\dot{\beta}$ and $\dot{\alpha}$.

REFERENCES

[1] F. Qiu and B. Nelson. *Magnetic Helical Micro-and Nanorobots: Toward Their Biomedical Applications*. Engineering, vol. 1, no 1, pp. 21-26, 2015.
[2] F. Qiu, S. Fujita, R. Mhanna, L. Zhang, B. Simona and B. Nelson. *Magnetic Helical Microswimmers Functionalized with Lipoplexes for Targeted Gene Delivery*. Advanced Functional Materials, vol. 25, no. 11, pp. 1666-1671, 2015.
[3] S. Tottori, L. Zhang, F. Qiu, K. Krawczyk, A. Franco-Obregn, and B. Nelson. *Magnetic helical micromachines: Fabrication, Controlled Swimming, and Cargo Transport*. Advanced Materials, vol. 24, no. 6, pp. 811-816, 2012.
[4] E. Purcell. *Life at low reynolds number*. American Journal Physics, vol. 45, no. 1, pp. 3-11, 1977.
[5] A. Aguiar and J. Hespanha. *Trajectory-Tracking and Path-Following of Underactuated Autonomous Vehicles With Parametric Modeling Uncertainty*. IEEE Transactions on Automatic Control, vol. 52, no. 8, pp. 1362-1379, 2007.
[6] A. Mahoney, J. Sarrazin, E. Bamberg and J. Abbott. *Velocity Control with Gravity Compensation for Magnetic Helical Microswimmers*. Advanced Robotics, vol. 25, no. 8, pp. 1007-1028, 2011.
[7] K. Peyer, L. Zhang, B. Kratochvil and B. Nelson. *Non-ideal Swimming of Artificial Bacterial Flagella Near a Surface*. IEEE International Conference on Robotics and Automation, pp. 96-101, Alaska, USA, 2010.
[8] T. Xu, G. Hwang, N. Andreff and S. Régnier. *Characterization of Three-dimensional Steering for Helical Swimmers*. IEEE International Conference on Robotics and Automation, pp. 4686-4691, 2014.
[9] T. Xu, G. Hwang, N. Andreff and S. Régnier. *Planar Path Following of 3-D Steering Scaled-Up Helical Microswimmers*. IEEE Transactions on Robotics, vol. 31, no. 1, pp. 117-127, 2015.
[10] A. Ghosh, D. Paria, G. Rangarajan and A. Ghosh. *Velocity Fluctuations in Helical Propulsion: How Small Can a Propeller Be*. Journal of Physical Chemistry Letters, vol. 5, no. 1, pp. 62-68, 2014.
[11] T. Oliveira, P. Encarnaao and A. Aguiar. *Moving Path Following for Autonomous Robotic Vehicles*. European Control Conference, pp. 3320-3325, Zrich, Switzerland, 2013.
[12] P. Encarnaao and A. Pascoal. *3D Path Following for Autonomous Underwater Vehicle*. IEEE Conference on Decision and Control, pp. 2977-2982, Sydney, Australia, 2000.
[13] C. Samson. *Control of chained systems application to path following and time-varying point-stabilization of mobile robots*. IEEE Transactions on Automatic Control, vol. 40, no. 1, pp. 64-77, 1995.
[14] L. Bushnell, D. Tilbury and S. Sastry. *Steering Three-Input Chained Form Nonholonomic Systems Using Sinusoids: The Fire Truck Example*. The International Journal of Robotics Research, vol. 14, no. 1, pp. 366-381, 1995.
[15] G. Walsh and L. Bushnell *Stabilization of multiple input chained form control systems*. Systems & Control Letters, vol. 25, no. 3, pp. 227-234, 1995.
[16] T. Xu, G. Hwang, N. Andreff and S. Régnier. *Modeling and Swimming Property Characterizations of Scaled-Up Helical Microswimmers*. IEEE/ASME Transactions on Mechatronics, vol. 19, no. 3, pp. 1069-1079, 2014.